Uppermost mantle seismic velocity and anisotropy in the Euro-Mediterranean region from *Pn* and *Sn* tomography

J. Díaz, A. Gil and J. Gallart

Institute of Earth Sciences J. Almera, ICTJA-CSIC c/Sole Sabaris s/n, 08028 *Barcelona, Spain. E-mail: jdiaz@ictja.csic.es*

SUMMARY

In the last 10–15 years, the number of high quality seismic stations monitoring the Euro-Mediterranean region has increased significantly, allowing a corresponding improvement in structural constraints. We present here new images of the seismic velocity and anisotropy variations in the uppermost mantle beneath this complex area, compiled from inversion of *Pn* and *Sn* phases sampling the whole region. The method of Hearn has been applied to the traveltime arrivals of the International Seismological Center catalogue for the time period 1990–2010. A total of 579 753 *Pn* arrivals coming from 12 377 events recorded at 1 408 stations with epicentral distances between 220 km and 1 400 km have been retained after applying standard quality criteria (maximum depth, minimum number of recordings, maximum residual values . . .). Our results show significant features well correlated with surface geology and evidence the heterogeneous character of the Euro-Mediterranean lithosphere. The station terms reflect the existence of marked variations in crustal thickness, consistent with available Moho depths inferred from active seismic experiments. The highest *Pn* velocities are observed along a continuous band from the Po Basin to the northern Ionian Sea. Other high velocity zones include the Ligurian Basin, the Valencia Trough, the southern Alboran Sea and central part of the Algerian margin. Most significant low-velocity values are associated to orogenic belts (Betics, Pyrenees, Alps, Apennines and Calabrian Arc, Dinarides-Hellenides), and low-velocity zones are also identified beneath Sardinia and the Balearic Islands. The introduction of an anisotropic term enhances significantly the lateral continuity of the anomalies, in particular in the most active tectonic areas. *Pn* anisotropy shows consistent orientations subparallel to major orogenic structures, such as Betics, Apennines, Calabrian Arc and Alps. The *Sn* tomographic image has lower resolution but confirms independently most of the features evidenced in the *Pn* tomography.

Key words: Tomography; Mantle processes; Body waves; Seismic anisotropy; Seismic tomography; Dynamics: seismotectonics; Europe.

1 INTRODUCTION

The uppermost mantle beneath the Euro-Mediterranean region is here investigated in terms of *Pn* and *Sn* tomography, based on the technique developed by Hearn (1996) which provides information on lateral seismic velocity variations, anisotropic properties and crustal thicknesses. Due to the shallow velocity gradient in the uppermost mantle and to the large contrast with lower crust velocities, *Pn* and *Sn* phases are confined in depth and thus the analysis of their traveltime variations provides insights on the velocity variations in the uppermost mantle. This methodology complements global and regional body-wave tomographies, that average velocity changes over large depth intervals and are very dependent of the crustal correction term as well as surface-wave studies, which provide good vertical resolution but tend to smooth variations horizontally. The observed variations in the *Pn* and *Sn* velocities can be associated to changes in the temperature, pressure, composition, or water con-

tent conditions. The anisotropic parameters to be derived from such kind of analysis constrain the mantle dynamics, as they can be related to the alignment of aggregate olivine crystals. Therefore, this method provides significant clues on the structure and dynamics of the uppermost mantle region.

The original purpose of this study was to apply this method to the Iberian Peninsula and Northern Morocco, in the framework of a number of projects currently on-going in that area, such as TopoIberia (Díaz *et al.* 2009), Picasso (Platt *et al.* 2008) or Rifsis (Gallart *et al.* 2012). However, we decided to extend the study area to cover the whole Euro-Mediterranean region (Fig. 1), with the aim of providing a view of the properties of the uppermost mantle beneath the whole region, affected by recent tectonic events including subduction and extensional processes. This large-scale approach allows integrating previous works focusing at smaller scales (Mele *et al.* 1998; Hearn 1999; Serrano *et al.* 2005) and to connect them with recently published *Pn* tomographies beneath East Asia
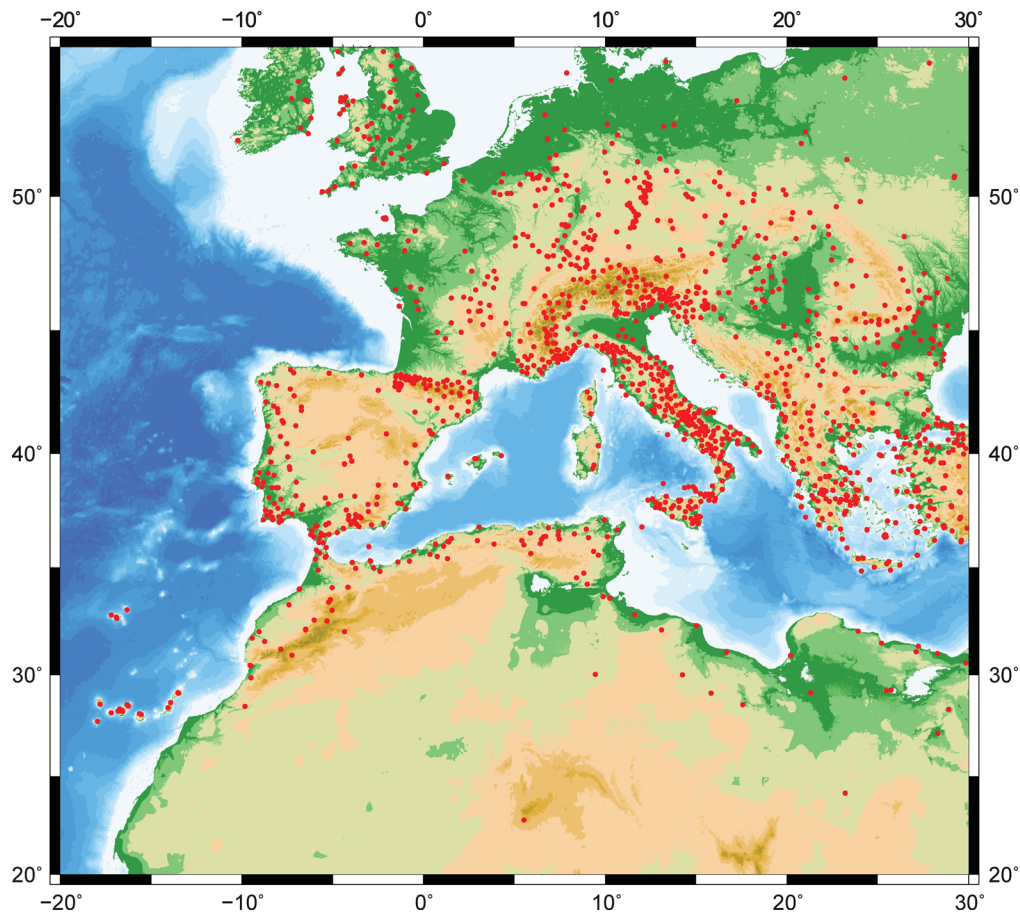
Figure 1. Topographic map of the study area including all the seismic stations used.

(Al-Lazki *et al.* 2004; Mutlu & Karabulut 2011) and the continental collision zone from Alps to Himalaya (Pei *et al.* 2011a). The lack of available seismic stations make impossible to extend the tomographic images southwards of the Mediterranean coasts of Africa. However, the Mediterranean basin is generally well sampled, as it will be discussed hereafter.

The investigated region has a complex geodynamic history. After the Variscan orogeny, a large rifting episode affected the Mediterranean region in Mesozoic times. Later on, during the late Mesozoic, the area was dominated by subduction zones of relatively short wavelength, which consumed the previous Tethyan oceanic crust and its continental margins. Since Cenozoic times, the tectonics is dominated by the opening of small-size oceanic domains in backarc situation in the framework of an Africa–Eurasia convergence. The main subduction zones surrounding the Mediterranean Basin are the Alps-Betics, the Apennines-Maghrebides and the Dinarides-Hellenides-Taurides, which have been imaged as high velocity slabs within the upper mantle in global and regional body-wave tomographies (Bijwaard & Spakman 2000; Piromallo & Morelli 2003; Koulakov *et al.* 2009; Giacomuzzi *et al.* 2012; Zhu *et al.* 2012). Extensional processes affected the whole region in Neogene times, as has been evidenced by the observation of a shallow asthenospheric layer in *S*-velocity tomographies (Marone *et al.* 2004; Schmid *et al.* 2008; Boschi *et al.* 2009; Legendre *et al.* 2012). Those extensional processes resulted in the opening of the Alboran, Algerian, Valencia and Provençal basins in the West, the Tyrrhenian and Ionian basins in the central Mediterranean, the Aegean basin in the East and the Pannonian basin at the northern limit of the investigated area. The origin of the Tyrrhenian and Alboran Seas is related to the fast roll-

back migration of the former West Mediterranean subduction zone that resulted in the Calabrian and Gibraltar arcs migrating East and Westwards, respectively. During this process, the Corsica and Sardina block, originally located close to NE Spain, underwent a 30° counter-clockwise rotation in Late Oligocene–Early Miocene, while the Balearic Islands underwent 25° of clockwise rotation. Since Neogene times, Africa is converging relative to Europe at a rate of about 5 mm yr^{-1}, as has been evidenced by space geodesy data. The direction of the relative motion between both plates is not completely understood, with a dominant NW–SE direction in the western Mediterranean and a NNE–SSW direction to the East. This framework resulted in a complicated tectonic pattern dominated nowadays by large regions of extension surrounded by arcuate belts of compression (Carminati & Doglioni 2005).

The geodynamics of the Euro-Mediterranean region has been a subject of debate during the last decade. Key questions, as the Cenozoic evolution of the western Mediterranean, the geometry of the subduction beneath the Peloponnesus or the relationship between the European and the Adria plates beneath the western Alps are still not solved. One of the main tools to investigate those points is provided by body and surface wave tomographies. However, those methods do not allow constraining properly the uppermost mantle, leading to relevant uncertainties in the geodynamic interpretation. Our new regional scale *Pn* and *Sn* tomographic inversions aims to provide new clues to the discussion of those open subjects.

2 DATA

We use time arrivals reported at the International Seismological Center (ISC) catalogue (International Seismological Centre

a)

b)
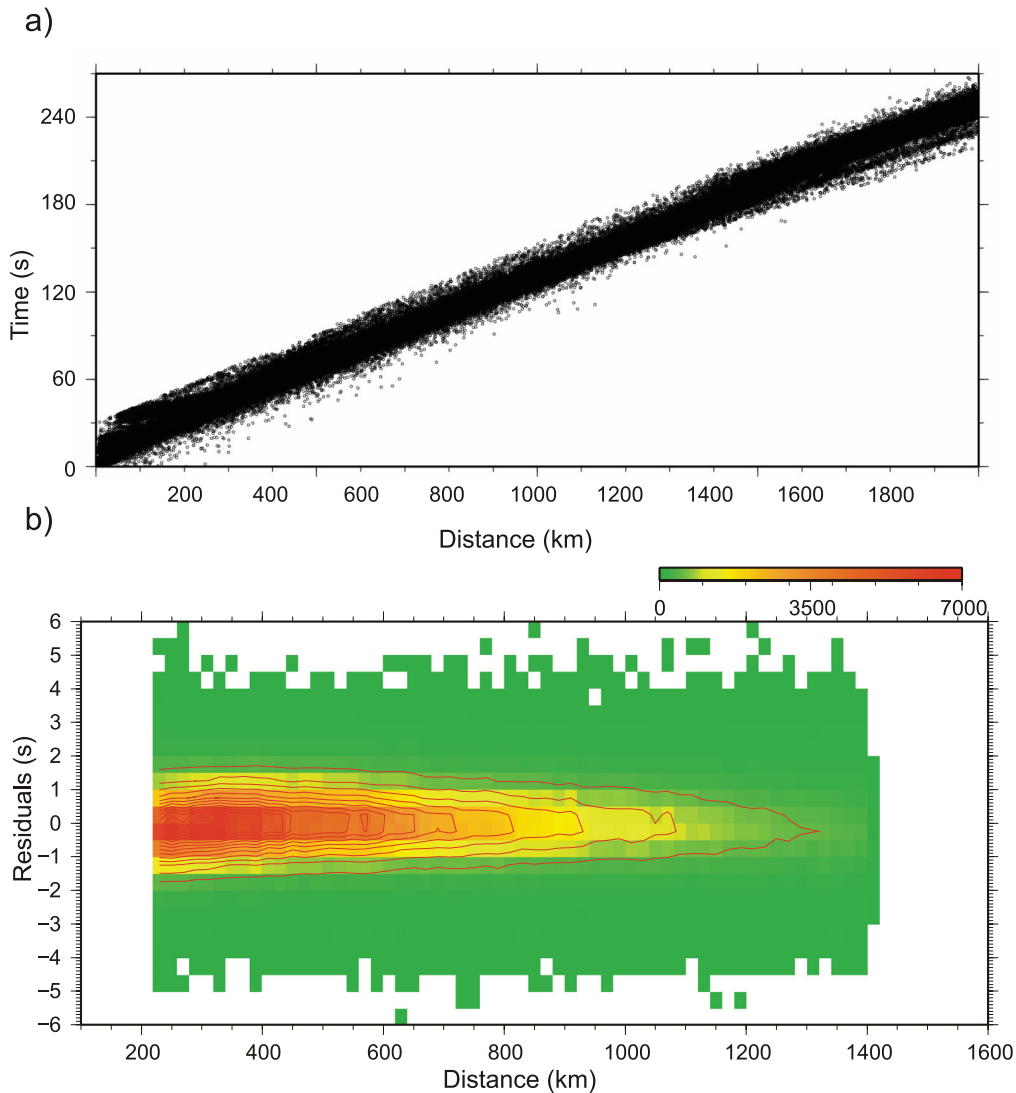
Figure 2. (a) Total traveltimes used in this study as a function of distance. (b) Retained traveltime observations as a function of the distance and the residual time (difference between the measured time and the theoretical one assuming $V_p = 8.0 \, \text{km s}^{-1}$). Colour scale and contours account for the number of retained observations.

2010) during the time interval 1990–2010, with epicentres and/or recording stations within the 20°N/55°N–30°W/30°E region. We have tried to extend the southward limit of the investigated area, but the lack of seismic stations southward of the Tell Atlas chain does not allow recovery of appropriate *Pn* phases. Data prior to 1990 has not been included because the number of available seismic stations has grown significantly in the last decades, providing great increase in the amount of observations and thus in the accuracy of the catalogues. We estimate that using the whole time range of the catalogue may have a negative effect because although the number of traveltime readings increases, its accuracy clearly decreases. The phases with traveltimes exceeding by more than 30 s the theoretical time have been excluded to avoid readings affected typically by 1-min errors. Fig. 2(a) shows the traveltime arrivals recovered from the catalogue.

Pn phases are defined as head waves travelling within the uppermost mantle just beneath the Moho discontinuity, with velocities close to 8.0 km s⁻¹. However, in an area geodynamically very complex such as the Mediterranean region, it is very difficult to clearly identify such waves. Following classical approaches, we assumed

that any phase which traveltime verifies appropriate selection criteria may be treated as a real *Pn* phase. These selection criteria are: (1) hypocentral depths less than 35 km; this avoids considering subcrustal earthquakes which will not generate *Pn* phases. We have chosen a realistic reference value, even if changes in crustal depths beneath the Mediterranean region are very important; (2) epicentral distances ranging from 220 to 1440 km (2.0° to 12.60°); those values were determined from the inspection of the time-distance plot of all available wave picks; (3) initial residuals smaller than 6 s; (4) residuals smaller than 3 s after the adjustment of the mean *Pn* velocity; (5) each retained event must be recorded at a minimum of five stations and each retained station must have arrivals from five or more events. These selection criteria have also been considered for the *Sn* phases, assuming a typical V_p/V_s ratio of 1.73.

Applying those constraints, from an initial set of 1 172 293 traveltimes, a total of 579 753 *Pn* arrivals corresponding to 12 377 events recorded at 1408 stations were retained for *Pn* waves (Fig. 2b), and 162 645 arrivals from 7528 earthquakes at 869 stations for *Sn* waves. The resulting ray paths provide an appropriate coverage for the *Pn* phases, although less satisfactory for the *Sn* ones (Fig. 3).
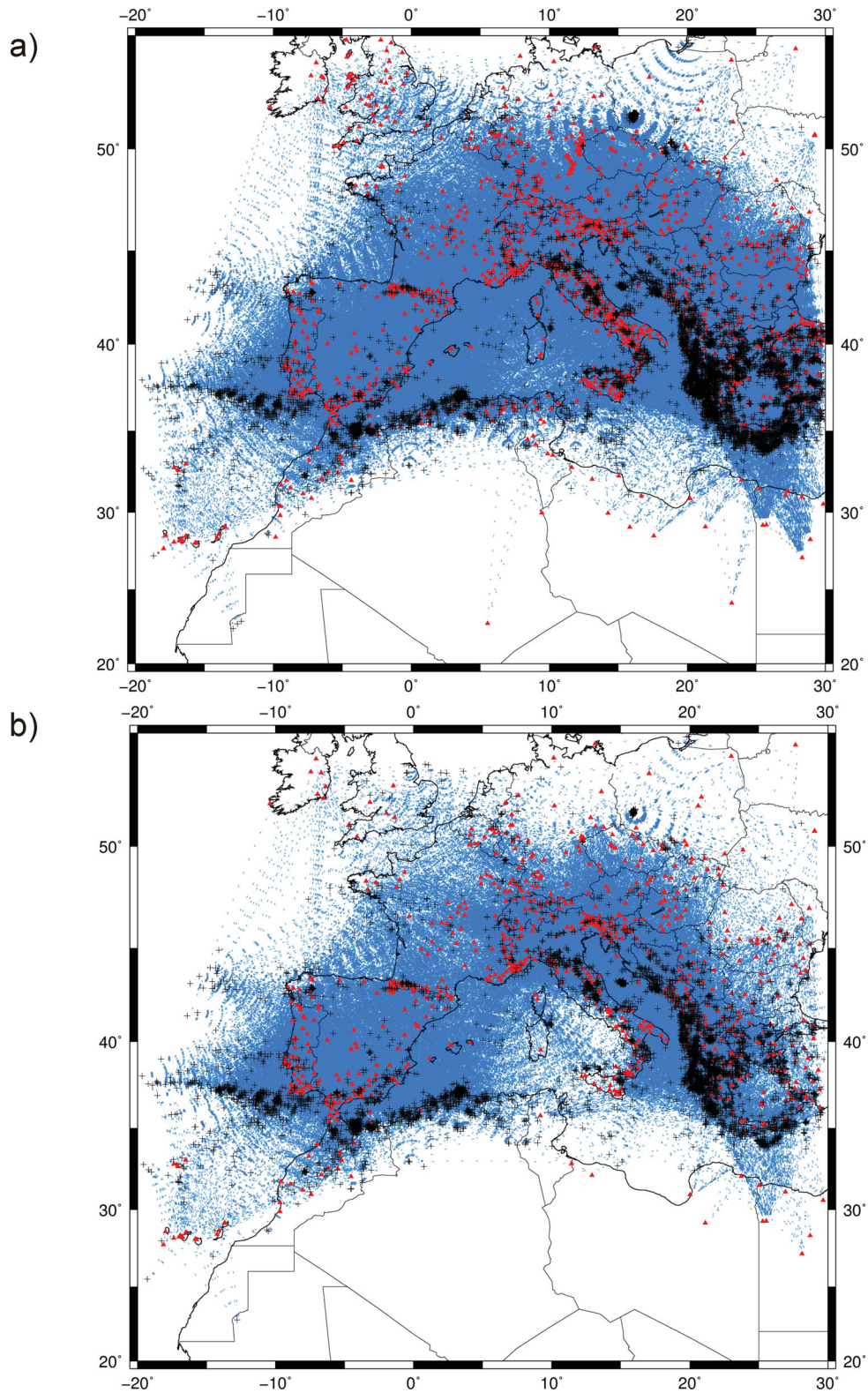
Figure 3. *Pn* (a) and *Sn* (b) ray paths used in our tomographic inversion. Red triangles and crosses display respectively the stations and events used in each tomographic inversion.

3 METHOD

We followed the classical method of Hearn (1996) for inverting *Pn* and *Sn* traveltimes both for isotropic velocity variations and transverse anisotropy perturbations.

If no anisotropy is considered, the traveltime between the *i* event and the *j* station can be expressed as

$$t_{ij} = a_i + b_j + \Sigma d_{ijk}s_k,$$

where a_i and b_j are, respectively, the static delays for event i and station j, d_{ijk} is the distance travelled by the ray within cell k and s_k is the slowness $(1/v)$ in this cell. The station delay depends on the crustal thickness and the velocity beneath the station, but may also include errors derived from timing problems or from erroneous picking of the phase arrivals. The event term can, in addition, contain the effect of mislocations of the event.

The sum is calculated over all the cells traversed by the ray, and the three unknowns a_i, b_j and s_k are retrieved from the whole set of equations using regularized least squares with a preconditioned version of the LSQR algorithm (Paige & Saunders 1982), which requires the use of a regularization or damping parameter. Further details of the technique can be found in Hearn & Ni (1994) and Hearn (1996). Thus, features and smoothness of the final model depend on the chosen size of the cells and the value of the smoothing parameter used.

Previous works have already shown than better results are obtained if we consider the presence of anisotropy. In this case, the equation to solve will be

$$t_{ij} = a_i + b_j + \Sigma d_{ijk} \left(s_k + A_k \sin 2\theta + B_k \cos 2\theta \right)$$

assuming that the anisotropy in the uppermost mantle can be properly described by a 2θ azimuthal term. A_k and B_k are the anisotropic parameters for cell k and θ is the backazimuth. The size of the anisotropy at cell k is related to $\left(A_k^2 + B_k^2 \right)^{1/2}$ and the azimuth of the fast direction of propagation will be given by $\frac{1}{2} \arctan(B_k/A_k) + 90°$. In this case, two damping factors must be used, one controlling the smoothness of the slowness variations and the other taking care of the anisotropy variations. The ratio between both factors controls the relative weight of the data variance accounted on each kind of variations, and both factors are used to get the right balance between low errors and small resolution width.

The anisotropic term in 2θ in the Hearn's equations is adapted from the theoretical work of Backus (1965) discussed in the classical review work by Crampin (1981). For *P* waves, the dependence on θ is

$$\rho V_p^2 = A + B_c \cos 2\theta + B_s \sin 2\theta + C_c \cos 4\theta + C_s \sin 4\theta,$$

where ρ is the density, and A, B_c, B_s, C_c and C_s are combinations of the elastic tensor (see eq. 6.2 on Crampin 1981). In the Hearn's approximation, the terms in 4θ are not retained due to its small contribution. For *S* waves, the equivalent equations are

$$\rho V_{SP}^2 = D + E_c \cos 4\theta + E_s \sin 4\theta$$

$$\rho V_{SR}^2 = F + G_c \cos 2\theta + G_s \sin 2\theta,$$

where V_{SP} and V_{SR} refer to the *S* waves polarized parallel and perpendicular to the symmetry plane. Assuming a horizontal symmetry plane, *SR* can be identified with the *SV* polarized phase, contained in the same plane than the *P* wave while *SP* will correspond to the *SH* component. Therefore, the *SV* polarized wave has a velocity variation with a 2θ dependence, in a very similar way to *P* waves, while the *SH* component will vary with 4θ. Introducing a 2θ anisotropic term in the *Sn* tomographic inversion implies the assumption that the *S* wave arrivals identified in the catalogues corresponds to *SV* polarized phases. This hypothesis is not unrealistic, as quite often the *S* wave time arrivals are read in vertical components. Therefore we decided to explore this case, even if we are aware that results should be taken with caution.

We have performed a series of tests to investigate the resolution that can be obtained with our event-station data set, and to fix the

values of the number of iterations and the damping factors more convenient for our data set. First trials were performed in the isotropic case with a number of iterations limited to 25. Different damping values from 200 to 1000 were tested and finally a value of 500 was retained for slowness, even if no significant changes appear for dampings larger than 400. When dealing with *Sn* arrivals a smaller damping factor of 200 must be used to get a smooth image. In the anisotropic case, the trade-off between velocity and anisotropy variations has been checked using different combinations of slowness and anisotropy damping factors. However, neither the standard errors nor the tomographic images obtained show significant differences, if extreme combinations were avoided. We finally used the same value for both damping factors, as has been recommended by Hearn (1996). This choice implies that the amount of velocity and anisotropy perturbation is similar. We decided to extend our calculations to 100 iterations, even if little additional effect on the standard error or the velocity image is observed after 60 iterations. The final root mean square of the residuals is 0.83946 s. Allowing more iterations resulted in more contrasted and patched velocity anomalies, that in turn make more convenient to use a higher damping factor, finally fixed to 1000 for the *Pn* inversion and to 600 for the *Sn* case.

The *Pn* tomography method assumes than the waves are travelling subhorizontally below the Moho. In case of a significant velocity gradient in the uppermost mantle the ray paths would deviate from this assumption, diving in the mantle lid and thus sampling higher velocities. However, the retained traveltimes fit properly along an $8.0\,\mathrm{km\,s^{-1}}$ line (Fig. 2a), without evidences of relevant velocity changes. Furthermore, Fig. 2(b) shows that a large majority of the used ray paths are less than $600\,\mathrm{km}$ in length. It has been tested that the retained traveltimes for the *Sn* phases adjust properly a $4.6\,\mathrm{km\,s^{-1}}$ line.

Checkerboard test models with different pattern sizes and alternating values of $\pm0.25\,\mathrm{km\,s^{-1}}$ for low and high velocities were used to explore the resolution, with station and event delays set to zero. We calculated synthetic traveltimes using the same configuration of events and stations as in the real case and the same damping factors to test whether the input model can be recovered properly. The checkerboard with a $2° \times 2°$ pattern can be satisfactorily recovered for velocity variations in most of the investigated area (Fig. 4a). However, the scarce amount of seismic stations in Northern Africa results in a lack of resolution in the southern Mediterranean coasts. Most of southwestern Europe and the northernmost Morocco are well resolved even if beneath Northern Iberia and the Gulf of Cadiz, the resolution diminishes as most of the rays are oriented along single directions, resulting in elongated leaking. A checkerboard with $1° \times 1°$ cells can only be recovered properly in the zone more illuminated by seismic rays, comprising Central Iberia, Western Mediterranean Basin, SW of France, Italy, the Balkans and Greece.

Regarding the anisotropic pattern, the resolution is clearly lower (Fig. 5). In this case the synthetic model has anisotropic fast polarization directions (FPDs) oriented orthogonally in neighbour cells, with a 3 per cent degree of anisotropy. Checkerboard tests show how the inversion produces spurious oblique orientations at the corners of the cells, resulting in an image dominated by those artefacts when checkerboard cells of $2° \times 2°$ are used. Only when large cells of $4° \times 4°$ are used, the anisotropic pattern can be properly retrieved in most of the study area. This clearly shows that the anisotropic parameters are not properly constrained at small scales and thus their interpretation must be taken with special care, focusing only in large-scale features.
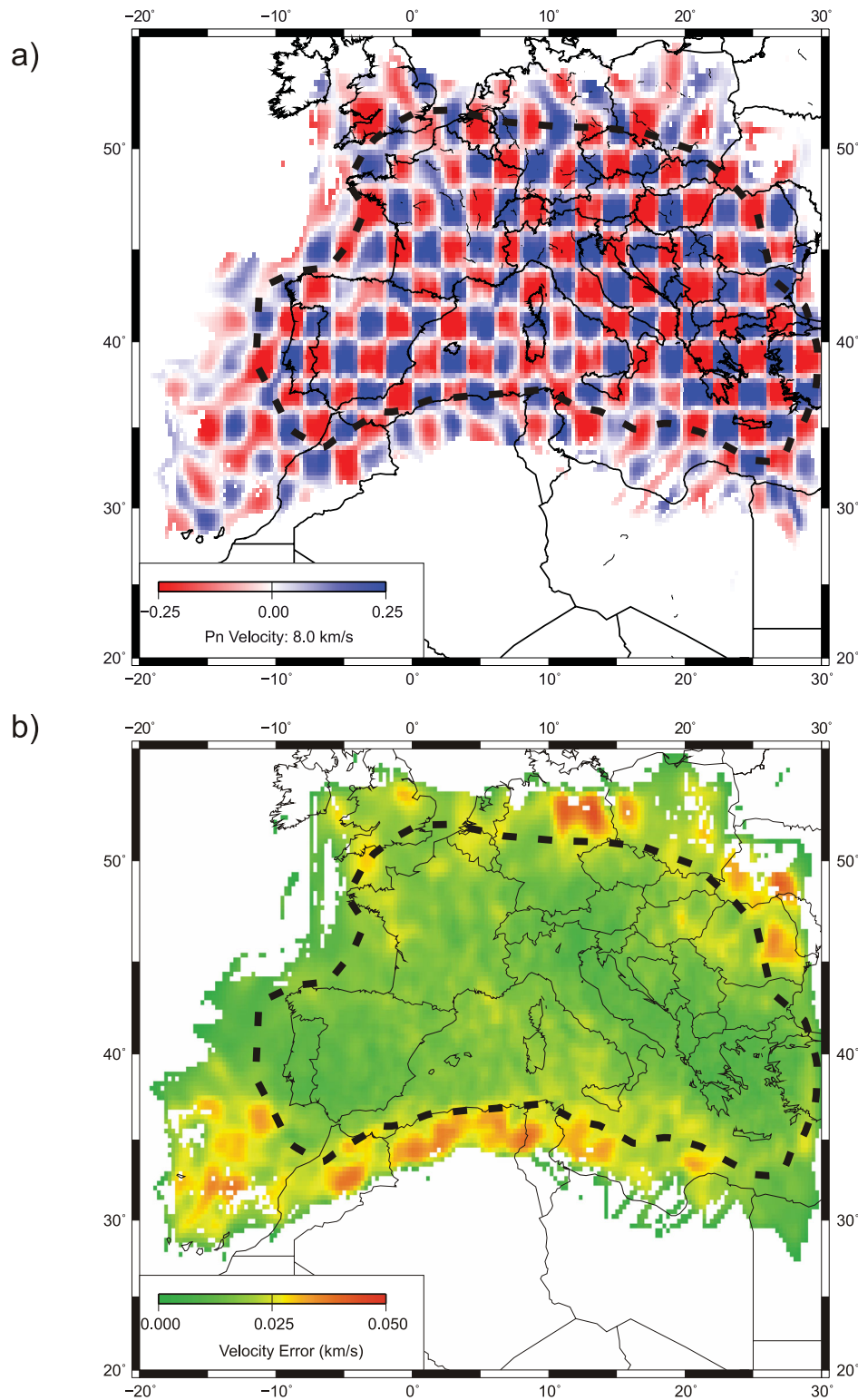
Figure 4. (a) Checkerboard test for *Pn* velocity variations (2° × 2°). (b) Standard deviations of the *Pn* velocity from bootstrap analysis. The dashed line delimits the confidence zone (small standard deviations of *Pn* velocity and successful checkerboard tests).

The bootstrap analysis technique (Hearn & Ni 1994) is used to estimate the errors in the *Pn* velocity distribution. The method works by constructing a number of data sets randomly picked from the original data, inverting each one with the same parameters and finally estimating statistically the standard error of the *Pn* velocity distribution. Fig. 4(b) shows the result of this procedure. The veloc-

ity errors are small, only exceeding $0.02 \, \mathrm{km \, s^{-1}}$ in the most external zones, thus confirming the good coverage in the central region.

Checkerboard test and bootstrap analysis have also been applied to the *Sn* data set (Fig. 6). In this case, the area recovered properly is smaller, due to the more limited number of traveltime readings. The main difference with *Pn* data is located beneath the Tyrrhenian
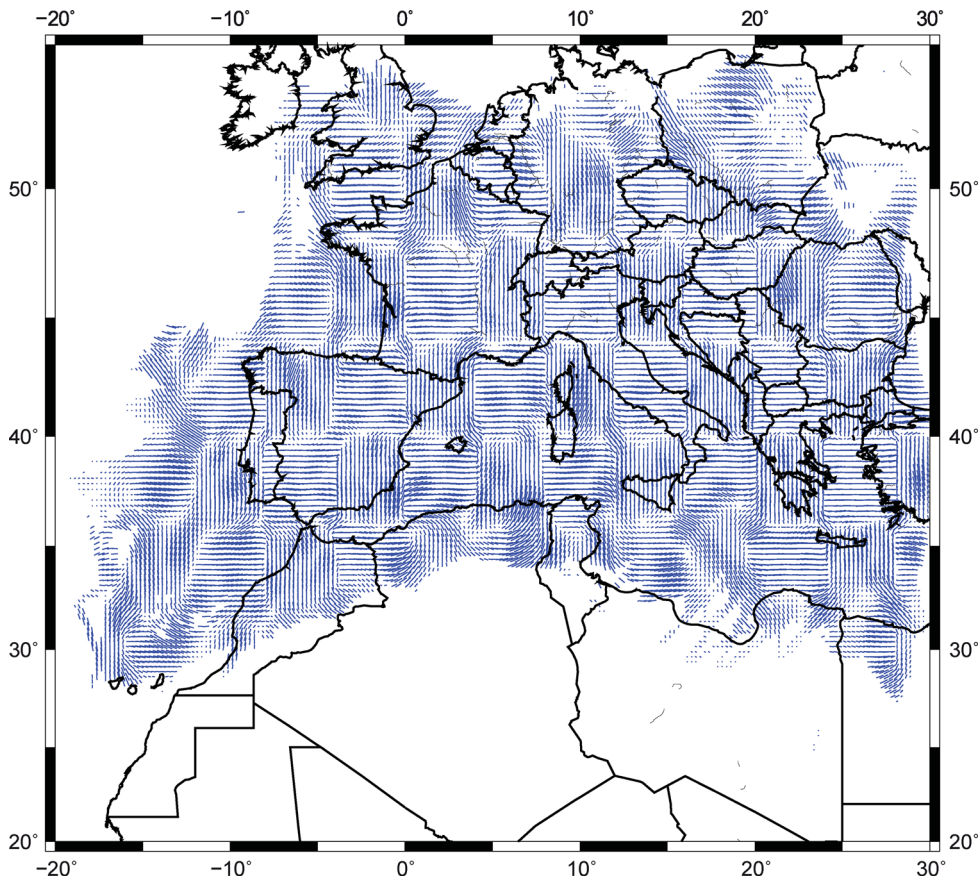
Figure 5. Checkerboard tests for anisotropic parameters in the *Pn* tomographic inversion (4° × 4°).

Sea, an area not sampled properly by *Sn* phases. However, a large zone including the whole Iberian Peninsula, France. Northern Italy, the Adria Plate, Central Europe, the Balkans and Greece is well resolved by both data sets.

4 RESULTS

The fitting of all the retained traveltimes led to a *Pn* velocity estimation of 8.03 km s^{-1}. Assuming a 6.2 km s^{-1} mean value for the crustal velocity, the obtained intercept time results in a mean crustal thickness over the whole area of 39.1 km.

The station static delay terms reflect variations in the crustal thickness and/or velocity relative to the assumed model. The presence of marked variations in crustal depth beneath the investigated area has been revealed from a large number of active seismic surveys (see Grad *et al.* 2009; Tesauro *et al.* 2008; Díaz & Gallart 2009, and references therein). The station delays obtained in our study (Fig. 7) are in general in good agreement with those results. Positive delays that can be related to zones with increased crustal thickness are observed along the Hellenides, Alps, Apennines, Pyrenees, Betics and Rif ranges. The largest consistent negative delays are observed from the Canary Islands to Sicily along the southern Mediterranean coasts.

The *Pn* velocity perturbations are calculated first for the isotropic case (Fig. 8a), and then an anisotropic term is introduced (Fig. 8b). At a first glance, the presence of heterogeneous lithospheric structures in the Mediterranean area is clearly inferred from the observation of very large fast and slow anomalies beneath the region, generally in close correlation with surface geology. The inclusion

of an anisotropic term does not improve significantly the final rms, evidencing the intrinsic trade-off between velocity and anisotropic variations. However, the anisotropic term enhances significantly the lateral continuity of the anomalies beneath the most active tectonic areas, as the Apennines and the Dinarides-Hellenides subduction belts and tends to focus the velocity anomalies, resulting in more contrasted images. This effect, already reported by Hearn (1996), suggests that the presence of anisotropy must be included in any seismic study to be carried over those regions.

The most significant low-velocity values (<7.8 km s^{-1}) are found beneath the main orogenic chains (Alps, Pyrenees, Betics, Apennines and the Calabrian Arc) and under the Sardinia and the East and South of the Balearic Islands, close to the northern limit of the Algerian Basin. The Dinarides-Hellenic arc is also imaged from its northern limit to the south of Peloponnesus Peninsula. Beneath Crete, the velocity anomaly is hardly recognized, probably due to reduced ray coverage. The signature of the Alps is not continuous, with low-velocity zones beneath its E and SW terminations, separated by an 8.0 km s^{-1} zone along the Swiss–Italian border. The anomaly beneath the Pyrenees is limited to its eastern section, while no perturbation is apparent neither in the western Pyrenean Chain nor beneath the westward prolongation of the orogen, the Cantabrian Mountains. However, the latter is not well sampled from our data. A large velocity anomaly is observed beneath the Eastern termination of the Betic chain, while the southern part of the Gibraltar Arc (Rif chain), still inside the well-resolved zone, shows a velocity close to 8.0 km s^{-1}.

The most prominent high velocity zone extends along the Adriatic Sea, from the Po Basin to the Ionian Sea. Less prominent high
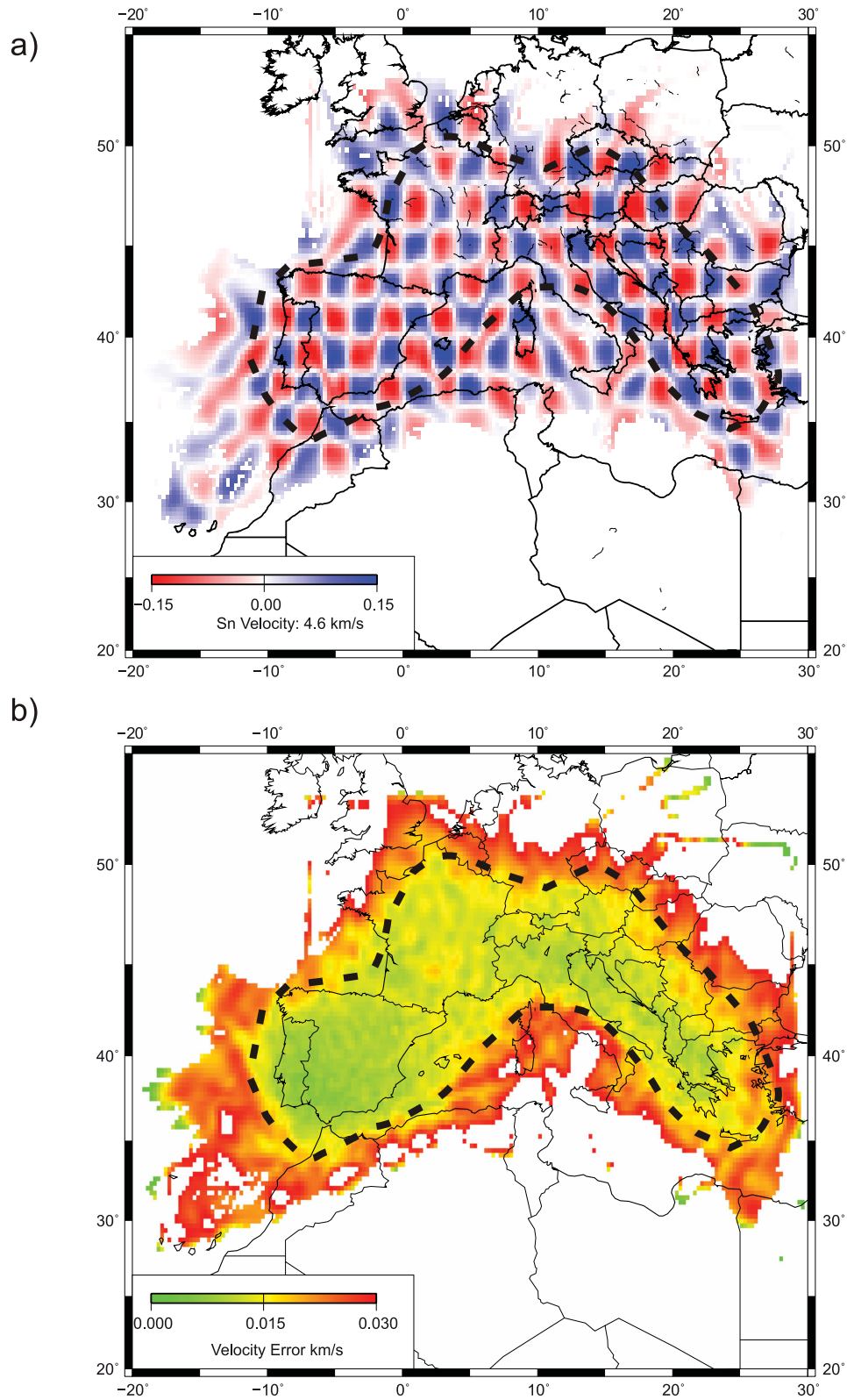
Figure 6. (a) Checkerboard test for *Sn* velocity variations (2° × 2°). (b) Standard deviations of the *Sn* velocity from bootstrap analysis. The dashed line delimits the confidence zone (small standard deviations of *Sn* velocity and successful checkerboard tests).

velocity zones appear under large sedimentary basins, as the Ligurian, Aquitanian or Guadalquivir-Rharb basins. The Kabylies, in the central and eastern coasts of Algeria, show another high velocity anomaly, while the Valencia Trough and the southern Alboran Sea

exhibit also a less pronounced but well-constrained high velocity anomaly.

The *Pn* tomographic image here obtained has a relatively good consistency with the uppermost layer of the available regional and
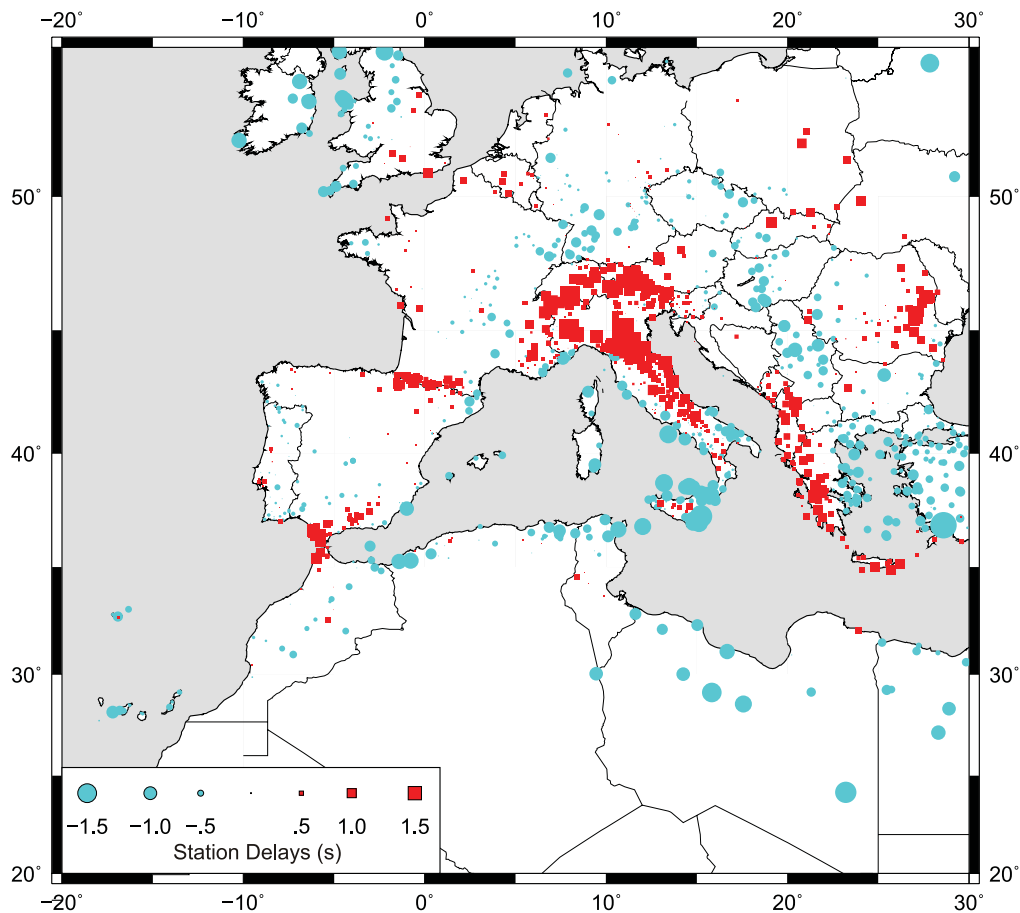
Figure 7. Static time delays associated to each station.

teleseismic 3-D tomographies (Bijwaard & Spakman 2000; Piromallo & Morelli 2003; Koulakov *et al.* 2009). The most prominent feature in both types of tomographic images is the low-velocity zones under the Dinarides-Hellenides, the Alps and the Apennines as well as the high velocity anomaly along the Po Basin and the Adriatic Sea. In the western Mediterranean, low velocities are observed south of the Balearic Islands and beneath the Betics. However, significant differences arise between the different tomographies in the Tyrrhenian and Provençal-Ligurian Basin, probably resulting from the lack of resolution in the upper layers in teleseismic tomography, which is greatly affected by abrupt variations in crustal thickness or velocity.

The resolution tests discussed in the previous section evidenced that the tomographic method here used allows to properly recovering only large-scale anisotropic features, as smaller ones may be the result of artefacts during inversion. Large anisotropy values (Fig. 9) appear beneath the Apennines, oriented subparallel to the belt and bending to NE–SW in the Calabrian Arc. The Alps show an arcuate variation of the anisotropic properties, from NS oriented FPD and a small degree beneath SE France to larger values and E–W oriented FPD under the Eastern Alps. Clear anisotropy with FPD subparallel to the orogen is also observed beneath the Dinarides and the Hellenides. The Betics have large anisotropy with FPD following the topography of the belt till the Strait of Gibraltar, but no clear evidences of anisotropy are observed beneath the Rif. In the Alboran Sea the FPD seem to shift smoothly from NS in the western part to NW–SE in its eastern section. Along the Valencia Trough, the magnitude of anisotropy is moderate and the FPD are parallel

to the extension. The FPD shifts around the Balearic Islands to a NE–SW orientation between the Balearic Promontory and Algeria, where the anisotropy is stronger. Beneath Sardinia, FPD are oriented NW–SE, changing abruptly to E–W under the Tyrrhenian Basin. Further North, another region with significant anisotropy is observed under southern Germany, an area still well-resolved by our data. The observed FPD are in this case oriented close to NNE–SSW. In general, the regions with high velocity anomalies do not show a consistent anisotropic pattern, while there is an overall correlation between the zones with a significant amount of anisotropy and those with low-velocity anomalies. For comparison purposes developed in the discussion section, Fig. 9(b) shows the available anisotropic results retrieved from *SKS* splitting in the study area.

For the inversion of the *Sn* phases, the same procedure has been considered, even if the number of traveltimes and the resulting ray coverage is clearly poorer (Fig. 3). In a first step, the inversion is done in the isotropical case. The results (Fig. 10a) show an overall similarity with the *Pn* inversion, even if some differences can be clearly observed. As discussed in Section 3, the inclusion of an anisotropic term, although not evident, produces an effect very similar to the case of *Pn* phases. The velocity perturbations are sharper and have more lateral continuity than if only isotropic velocity variations are allowed (Fig. 10b). This provides an *a posteriori* argument favouring the inclusion of an anisotropic term in the *Sn* velocity inversion. To better discuss the differences between the *Pn* and *Sn* velocity variations, Figs 11(a) and (b) show the V_p/V_s ratio calculated without and with anisotropic terms. Even if it has been shown that the
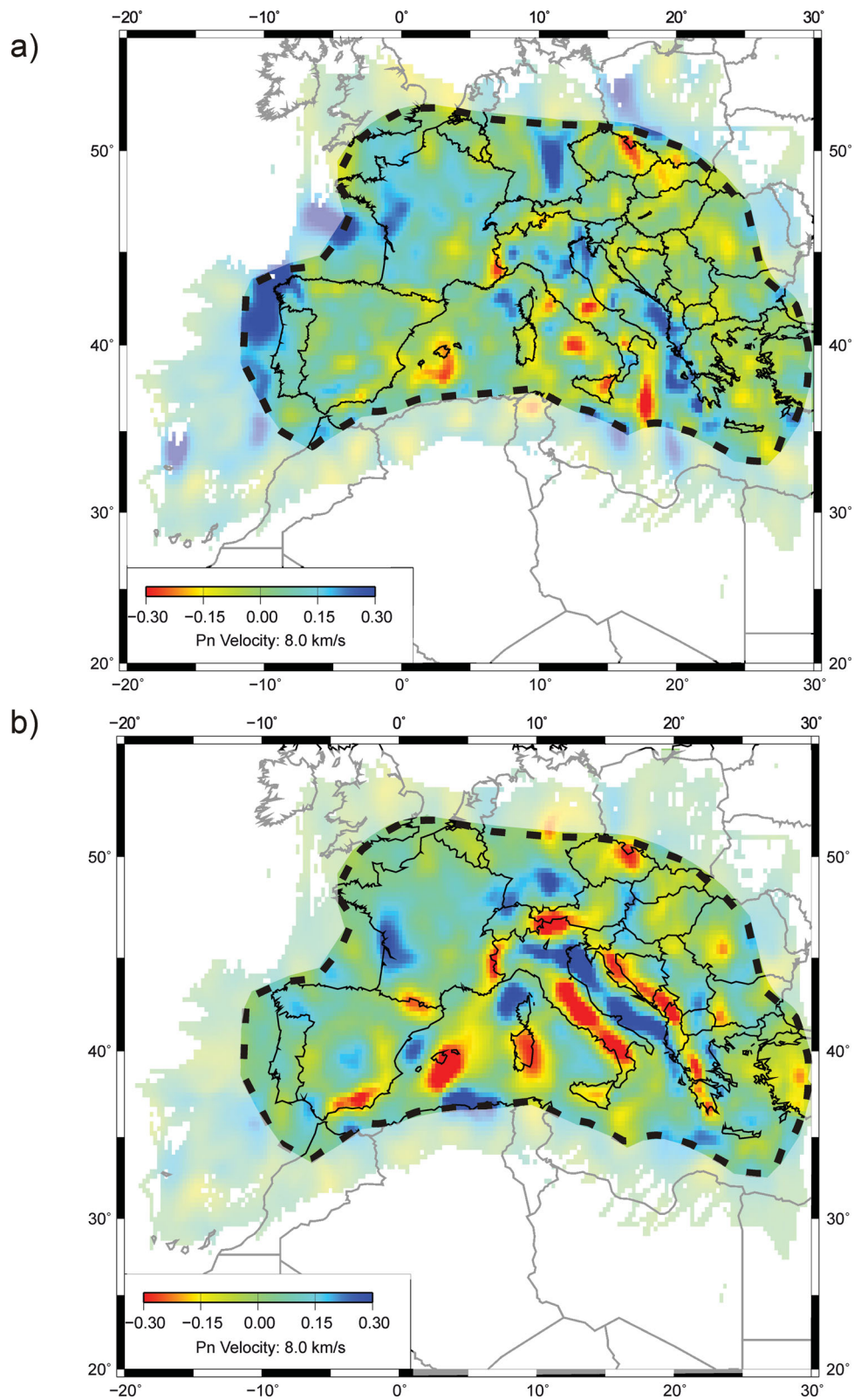
Figure 8. (a) *Pn* velocity anomalies with respect to $8.0\,\mathrm{km\,s^{-1}}$ assuming isotropic propagation (weight-damping factor: 1000). (b) *Pn* velocity anomalies including an anisotropic term (weight and anisotropic damping factors: 1000). The dashed line delimits the confidence zone; outside this area, the results are masked.
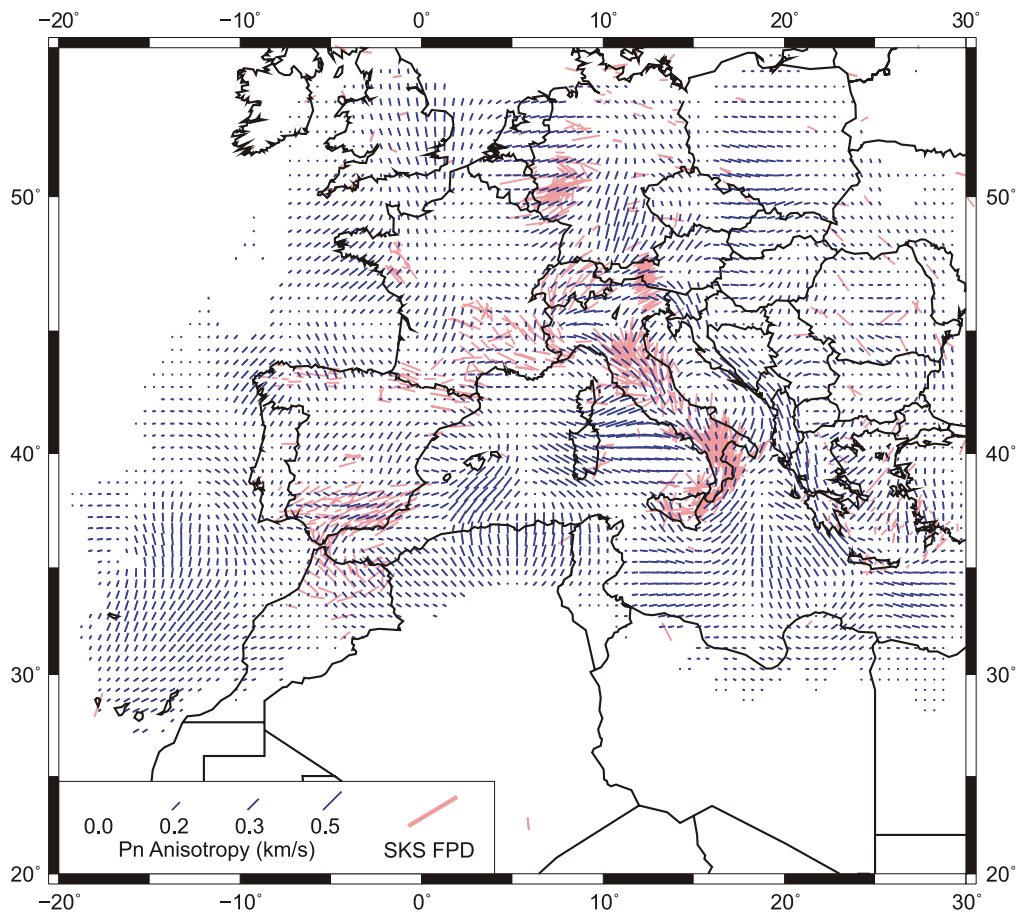
Figure 9. Anisotropic parameters recovered from the tomographic inversion. The orientation of the blue bars accounts for the fast polarisation directions in each cell. Its length show the strength of the anisotropy. Red bars correspond to the published anisotropic parameters in the Euro-Mediterranean region from the analysis of *SKS* splitting (Wüstefeld *et al.* 2009).

interpretation of V_p/V_s ratios in terms of Poisson ratio is difficult when the quality of the *P* and *S* velocities is significantly different (Eberhart-Phillips 1990), this representation provides a good tool to compare the *Pn* and *Sn* tomographic images. Within the area properly resolved by both *Pn* and *Sn* data, the more stable areas (Adria Plate, Central Iberia, France) have larger V_p/V_s ratios, while the active zones, including the Betics, Western Mediterranean, Alps, Dinarides and Hellenides display clearly smaller values.

5 DISCUSSION

Laboratory studies on peridotite samples at high-pressure conditions have shown that seismic velocities rapidly decrease with increasing temperatures (Sato *et al.* 1989). The presence of even small amounts of water can reduce the solidus temperature in the mantle, resulting in partial melt and low-seismic velocities (Karato & Jung 1998). Therefore, the low-velocity zones observed beneath the main orogenic belts suggest abnormally high temperature conditions, implying uppermost mantle material close to solidus and related to the building of the orogens. Compositional changes or the presence of some amount of water into the upper mantle as a result of the Neo-Tethys and Mediterranean lithosphere subductions may also explain such low values.

Mutlu & Karabulut (2011) have recently presented a *Pn* tomographic study of Turkey and adjacent regions, updating the previous

work by Al-Lazki *et al.* (2004) and showing low-velocity anomalies beneath western Anatolia, Aegean Sea and Greece. Pei *et al.* (2011a) obtained a large scale *Pn* and *Sn* tomography model extending from 15°E to the Himalaya. Beneath the Dinarides and the Aegean Sea those authors identify low velocities, while high velocities are observed beneath the southern section of the Adriatic Plate. The results here presented confirm these points, and thus make possible to extend the tomographic images till the Atlantic ocean, completing the imaging of the Alpine–Himalayan belt. As already proposed by Mele *et al.* (1998) using a limited number of traveltime readings, the large high velocity zone observed beneath the Po Basin and the Adriatic Sea may be due to its rather stable character, as it is widely accepted that stable cratonic areas result in high *Pn* velocity. The low-velocity area below the Dinarides-Hellenides can be associated to the presence of a mantle wedge (Hearn 1999). Below the Apennines, the low-velocity zones have probably a thermal origin related to its backarc position. It can be observed that the low-velocity zone in our results is limited to the Apennines and does not extend to the Tyrrhenian Sea as it has been imaged by teleseismic tomography (p.e., Koulakov *et al.* 2009). Beneath the Alps, the two important low velocities observed seem to be separated by a zone of normal velocity located roughly under the Insubric line, which marks the suture between the European and Adriatic plates. Lippitsch *et al.* (2003) using high-resolution tomography showed that at 90 km depth the velocity distribution is significantly different, with high velocities
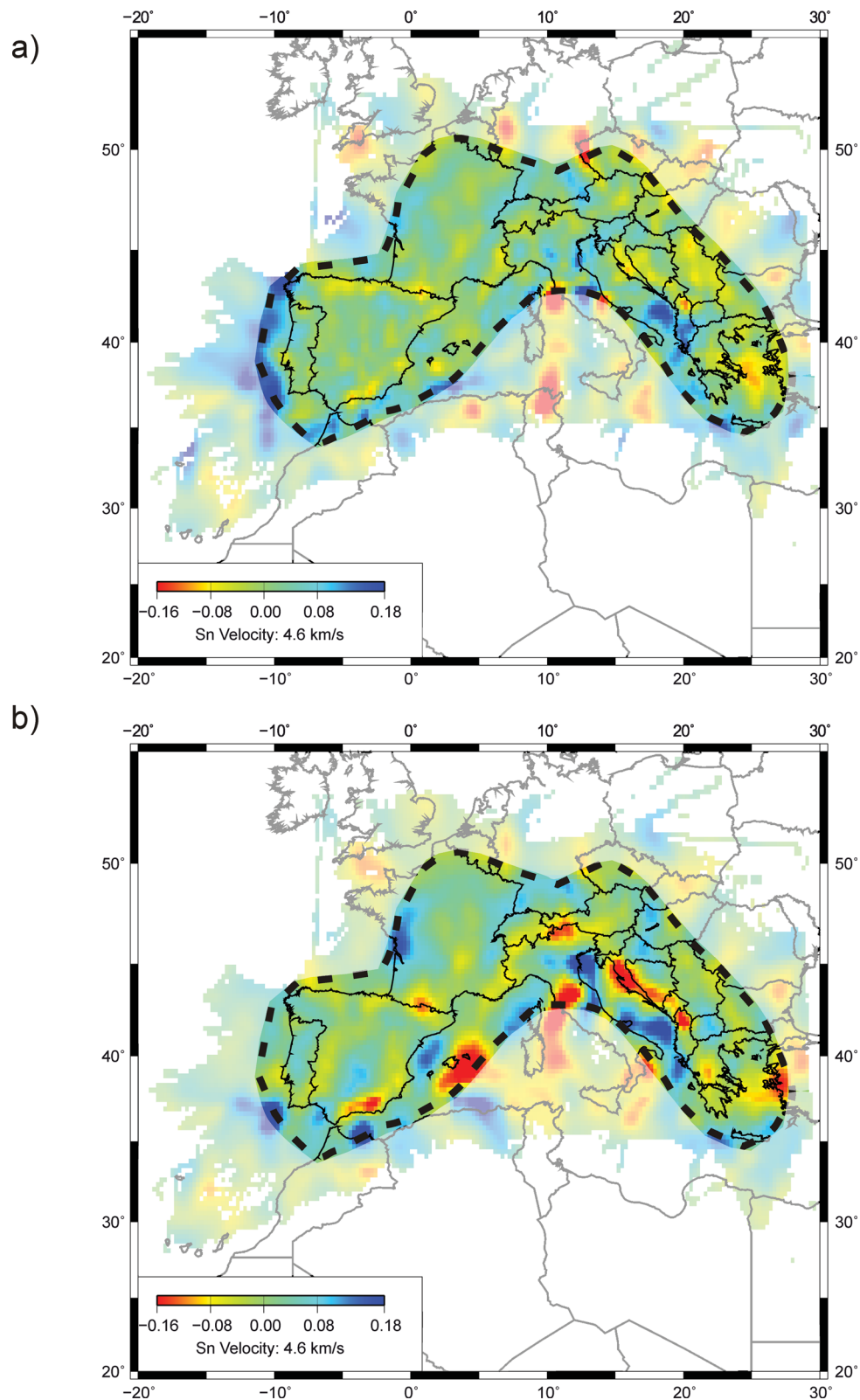
Figure 10. Obtained *Sn* velocity anomalies with respect to 4.6 km s^{-1} assuming isotropic propagation (a) and including also an anisotropic term (b). The damping factors are fixed to 600. The dashed line delimits the confidence zone; outside this area, the results are masked.

beneath SW Alps and the Adriatic Plate a low velocity beneath western Switzerland. The uppermost mantle beneath southern Germany shows a well defined high velocity anomaly already identified in a regional *Pn* tomography presented by Song *et al.* (2004) and

interpreted as resulting from an ancient process of underplating. Under the Pyrenees, the presence of low velocities only in its Central-Eastern section may reflect the different characteristics of the Alpine orogeny along the chain. The Alpine deformation begins
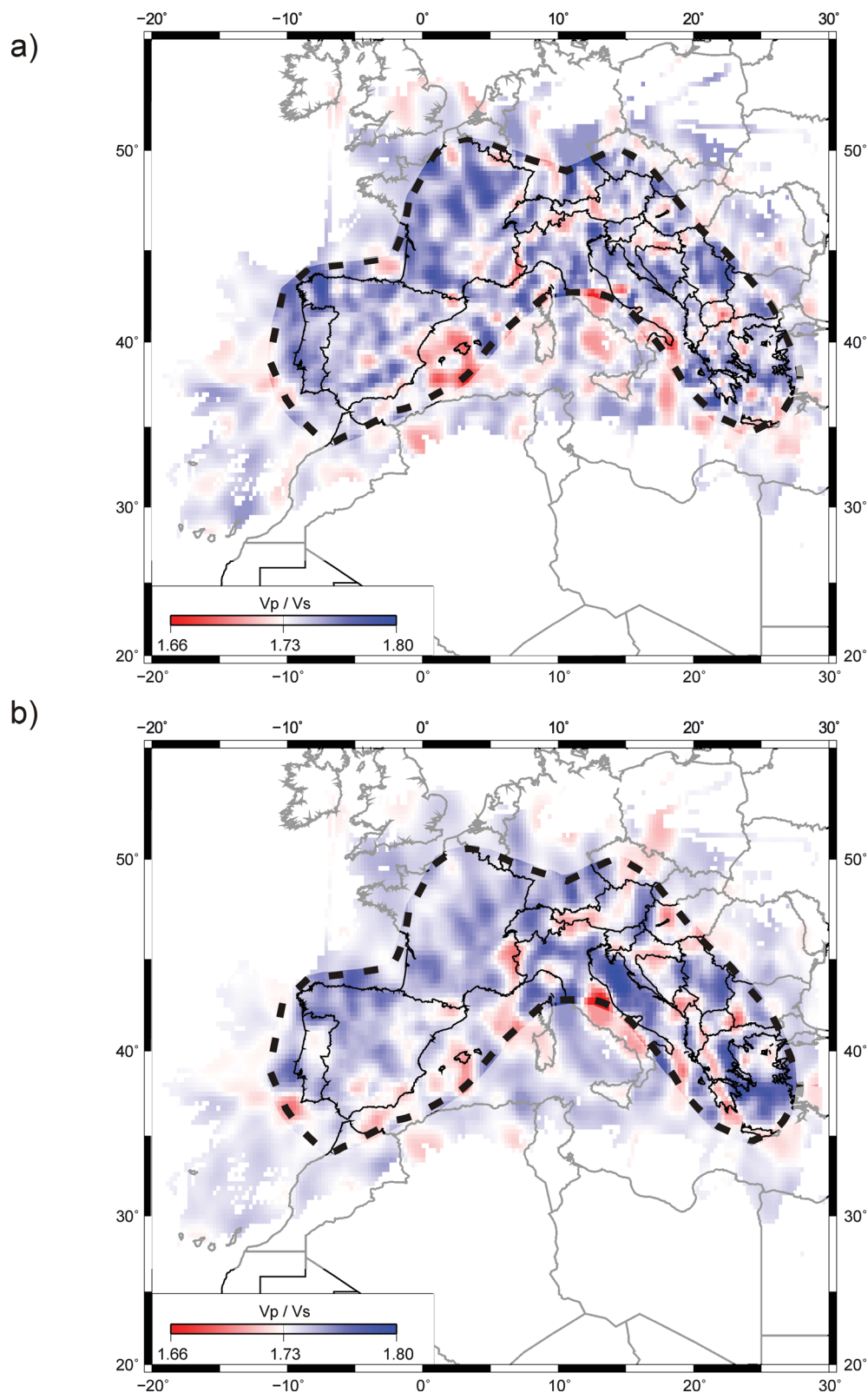
Figure 11. V_p/V_s ratios retrieved from the inversions assuming isotropic propagation (a) and including also an anisotropic term (b).

in the Late Cretaceous at the eastern Pyrenees (Vergés *et al.* 1995) and only in Eocene to Miocene times in the Cantabrian Mountains (Gallastegui *et al.* 2002). The shortening along the chain has been evaluated in 150 km in central Pyrenees (Muñoz 1992) but limited to 75 km in the western Pyrenees (Teixell 1998). Hence,

the low-velocity zone corresponds to the area where the Alpine deformation began first and where the shortening has been more important.

Active seismic surveys beneath the Betics (Banda & Ansorge 1980) have evidenced a low-velocity region beneath a thin

mantle lid. This region, located between 38–40 km and 60 km depth, is grossly consistent with the large low-velocity area observed in both *Pn* and regional and teleseismic tomographies and its origin should be related to hot mantle. Teleseismic wave tomography has identified a high velocity slab under the Alboran Sea at depths exceeding 100–150 km. Garcia-Castellanos & Villaseñor (2011) recently proposed a model that includes a lateral tear of this slab beneath the Betics, which may be consistent with our observation of low velocities beneath the Betics but not further south along the Gibraltar Arc. This region has been investigated using *Pn* phases by Calvert *et al.* (2000) and Serrano *et al.* (2005) using different sets of data, which had evidenced the presence of a robust low-velocity anomaly with significant anisotropy beneath the internal Betics. Calvert *et al.* (2000) observed a high velocity slab beneath the southern part of the Alboran Sea which was related to a rather cold mantle beneath this zone and which appears also in our results. However, heat flow data (Soto *et al.* 2008) does not seem compatible with this hypothesis, as it defines a hotter region (>650°C) at Moho depths running SW–NE across the central part of the Alboran Sea.

The observation and interpretation of the low-velocity zones close to the Balearic Islands and beneath Sardinia are of particular interest because, even if previous *S*-wave tomographies depicted the presence of a low-velocity zone in the Algero-Provençal and Tyrrhenian basins at depths of 75–100 km (Marone *et al.* 2004; Legendre *et al.* 2012), its presence at shallower levels has not been previously described. The Balearic Islands low-velocity zone is limited to the East by the Hannibal Ridge and includes the Emile Baudot escarpment, a large right-lateral transform zone oriented NE–SW and interpreted as marking the westward migration of the Alboran microplate (Acosta *et al.* 2001). Mauffret *et al.* (2004), suggested that the Hannibal ridge was an active spreading centre until Tortonian (8 Ma) or even after (6 Ma). Multibeam mapping led to the discovery of the SW Mallorca Volcanic Field, an area with a relevant number of volcanic pinnacles related to Miocene to recent volcanism (Acosta *et al.* 2001). Therefore, the observed low-seismic velocities are probably related to the presence of hot materials in the uppermost mantle associated to the recent tectonics in the area. The eastward migration of the volcanic arc associated to the counter-clockwise rotation of the Corsica-Sardinia block resulted in ongoing volcanism in Sardinia until 12 Ma, followed by a sporadic anorogenic phase developed during the Late Miocene-Quaternary (Beccaluva *et al.* 2011). Hence, here again the observed low-velocity zones are consistent with the presence of hot materials at shallow levels. The geometry of both low-velocity zones allow to speculate with an original unique low-velocity zone, split during the emplacement of the Corsica-Sardinia block. Many reconstructions of the Western Mediterranean suggest continuity between the subducted slabs beneath the Calabrian and the Gibraltar Arcs along the Algerian margin, even if global tomography images do not confirm this point (Rosenbaum *et al*. 2002). The high velocity anomaly beneath the Kabylies, observed both in our *Pn* results and in global tomographic images, can then be related to a segmented slab affected by vertical tearing.

Comparing V_p and V_s tomographies it can be observed that tectonically active zones tend to present smaller V_p/V_s ratios, while the stable areas have higher values. However, this point has to be taken with caution, as it has been show that the difference in the number and quality of the *Pn* and *Sn* observations makes difficult the interpretation of this ratio. Pei *et al.* (2011b) proposed an approach based in the backprojection of *S–P* time differences that can be used in future works to assess the validity of this result.

The presence of anisotropy within the upper mantle is nowadays well established (Babuska & Cara 1991). The origin of such anisotropy is related to the strain induced lattice preferred orientation (LPO) of the mantle minerals, in particular of olivine (p.e., Nicolas & Christensen 1987). Anisotropy thus provides one of the best tools to investigate deformation in the upper mantle somehow extending structural geology to depth. In tectonically active areas, FPD are expected to mark the direction of flow. In zones without present-day large-scale tectonic activity, LPO result from strain from the last significant tectonic episode preserved in the subcrustal lithosphere or from dynamic flow in the asthenosphere. During the last decades, the analysis of *SKS* splitting has provided a large amount of information related to mantle anisotropy. However, the relationship between the results of those studies and the anisotropic parameters retrieved from *Pn* tomography must be taken with caution, as significant resolution differences arise between both cases. *SKS* provides a good lateral resolution, only limited by the Fresnel zone beneath each station, but fails to constraint the deep location of the anisotropic zone. On the other hand, *Pn* tomography samples only the uppermost part of the mantle thus providing a good resolution in depth but its lateral resolution is limited, as it has been discussed in previous sections. Schmid *et al.* (2004) presented a compilation on FPD inferred from *SKS* splitting analysis over the Euro-Mediterranean zone. In the last years, new experiments have improved the knowledge on anisotropy over this region, as summarized in Fig. 9, build using the results compiled by the "SplittingDataBase" (Wüstefeld *et al.* 2009).

The good correlation between the inferred *Pn* FPDs and the trend of the main orogenic belts suggest that the origin of this anisotropy is related to the strain field. In the Aegean region the FPD tend to be oriented NE–SW (trench-perpendicular) in the backarc, where anisotropy is related to mantle wedge flow. Close to the trench, the FPD tend to be parallel to its orientation, even if the results show significant scattering (Evangelidis *et al.* 2011). The *Pn* anisotropic parameters obtained in our study show a similar pattern, with FPD clearly parallel to the trench and changing to a more scattered, roughly NE–SW orientation in the backarc region. Enderle *et al.* (1996) summarized the results from the large amount of deep seismic sounding profiles sampling southern Germany along different directions. They found 3–4 per cent anisotropy with FPD oriented N30°E below the Moho and changing slightly with depth. The results from our study are well consistent with this feature. In the Northern Apennines, the FPD derived from *SKS* splitting are oriented roughly parallel to the belt, even if some variations can be observed between the different domains (Salimbeni *et al.* 2008). The *Pn* results here presented show a very similar pattern, with a main NW–SE component but shifting to NNE–SSW in the Adria region and showing a large EW component beneath Tuscany. Large variations in the anisotropic parameters are observed in the Tyrrhenian Basin. While its central and southern part is dominated by a moderate, E–W oriented FPD, the northern edge, between Corsica and Italia, show a higher anisotropy with FPD oriented NE–SW to ENE–WSW. In the southern part of the Italic Peninsula, the observed FPD shows a clear rotation following the Calabrian Arc. The same pattern has been derived from *SKS* splitting and has been interpreted as the result of mantle flow around the subducting slab (Baccheschi *et al.* 2008). The anisotropic parameters obtained from *Pn* and *SKS* splitting are also very similar beneath the western Alps, with FPD following again the trend of the belt, from a NE–SW orientation to the North, to a roughly NS orientation in the southern termination of the Alps. Here again, the *SKS* results have been related to mantle flow around the subducted slab (Barruol

et al. 2011). The available anisotropic parameters retrieved from *SKS* splitting beneath the Pyrenees (Barruol *et al.* 1998) show a clear ESE–WNW orientation, while our results do not show any evidence of anisotropy, suggesting that its origin is deeper. *SKS* results in the Balearic Islands show a ESE–WNW FPD which clearly differs from the NE–SW oriented anisotropy appearing south of the islands in our work. This suggests again changes with depth of the anisotropic properties. Along the Gibraltar Arc, *SKS* results found a clear rotation of the FPD following the arc curvature, with similar strength in both terminations (Díaz *et al.* 2010). While the *SKS* results beneath the Betics are clearly consistent with the anisotropic properties inferred from *Pn* tomography, beneath northern Africa the results differ: *SKS* analysis show NW–SE oriented FPD, while *Pn*-derived fast directions are oriented NNE–SSW with intensity vanishing to the South. Beneath the Alhoceimas region, at the SE termination of the Arc, *SKS* data changes abruptly from NW–SE to NE–SW, while *Pn* FPD varies more smoothly and shows a NW–SE orientation beneath western Morocco and eastern Algeria.

The overall similarity between anisotropic parameters retrieved from *Pn* tomography and from the splitting of teleseismic *SKS* observed beneath some orogens (Betics, Apennines, Alps, Dinarides-Hellenides) suggests that the anisotropy is rather uniform from the base of the crust to deeps of about 300 km (the lower depth range where significant anisotropy is expected). In those cases, the anisotropic pattern may be explained by deformation in the subcrustal lithosphere beneath the orogens, with extension along the arc and compression orthogonal to it. Under those conditions, dewatering of the slab will create near solidus conditions in the mantle, hence explaining the low velocities observed beneath the orogenic belts. The hot temperatures will allow the lithospheric mantle to deform coherently, favouring the LPO and thus enhancing the anisotropy. Beneath some regions where an anisotropic origin related to mantle flow around subducted slab has been proposed (SE Alps, southern Gibraltar Arc) *Pn* and *SKS* anisotropic parameters clearly differ, suggesting different levels of anisotropy.

6 CONCLUSIONS

We presented new images of the seismic velocity and anisotropy variations in the uppermost mantle beneath the Euro-Mediterranean region obtained from the inversion of a large set of *Pn* and *Sn* arrivals compiled from the ISC catalogue for the 1990–2010 period. This contribution takes advantage of the increased number of observations available in the last decades in the Euro-Mediterranean region and provides for the first time an integrated image of the subcrustal *P*- and *S*-wave variations across the region. This contribution extends to the West the previous work by Pei *et al.* (2011a), hence providing a complete image of those variations all along the Alpine-Himalayan belt. The station delays depict the marked variations in crustal thickness also evidenced by active seismic experiments. The inclusion of an anisotropic term in the tomographic inversion clearly improves the lateral continuity of the velocity anomalies, confirming that the presence of anisotropy must be considered in seismic studies within this region. The highest *Pn* velocities are observed along a continuous band from the Po Basin to the northern Ionian Sea, while the most significant low-velocity values are associated to orogenic belts (Betics, Pyrenees, Alps, Apennines and Calabrian Arc, Dinarides-Hellenides) and probably related to thermal anomalies beneath the orogens. Large low-velocity zones are identified beneath Sardinia and the Balearic Islands, probably reflecting the presence of asthenospheric material at shallow levels. *Pn* anisotropy

shows consistent FPD orientations subparallel to major orogenic structures, such as Betics, Apennines, Calabrian Arc and Alps in agreement with the anisotropic parameters retrieved from teleseismic shear wave splitting. This similarity suggests that the anisotropy lies within the subcrustal lithosphere beneath the orogens. On the contrary, at some regions (South-East Alps, southern Gibraltar Arc) the anisotropy results inferred from the two methods clearly differ, suggesting that at least two anisotropic zones with different origin may exist. The *Sn* tomographic image has lower resolution but allows confirming independently most of the features evidenced in the *Pn* tomography. The overall velocity variations are similar to the *Pn* image, but the inspection of the V_p/V_s variations allow to associate the tectonically stable areas with increased V_p/V_s values and the most active ones with lower V_p/V_s ratios.

REFERENCES

Acosta, J., Munoz, A., Herranz, P., Palomo, C., Ballesteros, M., Vaquero, M. & Uchupi, E., 2001. Geodynamics of the Emile Baudot Escarpment and the Balearic Promontory, western Mediterranean, *Mar. Pet. Geol.,* **18,** 349–369.

Al-Lazki, A.I., Sandvol, E., Seber, D., Barazangi, M., Turkelli, N. & Mohamad, R., 2004. Pn tomographic imaging of mantle lid velocity and anisotropy at the junction of the Arabian, Eurasian and African plates, *Geophys. J. Int.,* **158,** 1024–1040.

Babuska, V. & Cara, M., 1991. Modern approach in geophysics, in *Seismic Anisotropy in the Earth*, Kluwer Academic publishers, London.

Baccheschi, P., Margheriti, L. & Steckler, M.S., 2008. SKS splitting in southern Italy: anisotropy variations in a fragmented subduction zone, *Tectonophysics,* **462,** 49–67.

Backus, G.E., 1965. Possible forms of seismic anisotropy of the uppermost mantle under oceans, *J. geophys. Res.,* **70,** 3429–3439.

Banda, E. & Ansorge, J., 1980. Crustal structure under the central and eastern part of Betic Cordilleras, *Geophys. J. R. astr. Soc.,* **63,** 515–532.

Barruol, G., Souriau, A., Vauchez, A., Díaz, J., Gallart, J., Tubia, J. & Cuevas, J., 1998. Lithospheric anisotropy beneath the Pyrenees from shear wave splitting, *J. geophys. Res.,* **103,** 30 039–30 054.

Barruol, G., Bonnin, M., Pedersen, H., Bokelmann, G.H.R. & Tiberi, C., 2011. Belt-parallel mantle flow beneath a halted continental collision: The Western Alps, *Earth planet. Sci. Lett.,* **302,** 429–438.

Beccaluva, L., Bianchini, G., Natali, C. & Siena, F., 2011. Geodynamic control on orogenic and anorogenic magmatic phases in Sardinia and Southern Spain: inferences for the Cenozoic evolution of the western Mediterranean, *Lithos,* **123,** 218–224.

Bijwaard, H. & Spakman, W., 2000. Non-linear global P-wave tomography by iterated linearized inversion, *Geophys. J. Int.,* **141,** 71–82.

Boschi, L., Fry, B., Ekström, G. & Giardini, D., 2009. The European upper mantle as seen by surface waves, *Surv. Geophys.,* **30,** 463–501.

Calvert, A., Sandvol, E., Seber, D., Barazangi, M., Vidal, F., Alguacil, G. & Jabour, N., 2000. Propagation of regional seismic phases (Lg and Sn) and Pn velocity structure along the Africa-Iberia plate boundary zone: tectonic implications, *Geophys. J. Int.,* **142,** 384–408.

Carminati, E. & Doglioni, C., 2005. Europe-Mediterranean tectonics, in Encyclopedia of Geology, Elsevier, Oxford, pp. 135–146.

Crampin, S., 1981. A review of wave motion in anisotropic and cracked elastic media, *Wave Motion,* **3,** 342–391.

Díaz, J. & Gallart, J., 2009. Crustal structure beneath the Iberian Peninsula and surrounding waters: a new compilation of deep seismic soundig results, *Phys. Earth planet. Inter.,* **173,** 181–190.

Díaz, J. *et al.*, 2009. The IBERARRAY broadband seismic network: a new tool to investigate the deep structure beneath Iberia, *Orfeus Newsl.*, **8**(2), 1–6.

Díaz, J. *et al.*, 2010. Mantle dynamics beneath the Gibraltar Arc (W Mediterranean) from shear-wave splitting measurements on a dense seismic array, *Geophys. Res. Lett.,* **37**(18), L18304, doi:10.1029/2010GL044201.

Eberhart-Phillips, D., 1990. Three-dimensional P and S velocity structure in the Coalinga region, California, *J. geophys. Res.,* **95,** 15 343–15 363.

Enderle, U., Mechie, J., Sobolev, S. & Fuchs, K., 1996. Seismic anisotropy within the uppermost mantle of southern Germany, *Geophys J. Int.,* **125**(3), 747–777.

Evangelidis, C.P., Liang, W.-T., Melis, N.S. & Konstantinou, K.I., 2011. Shear wave anisotropy beneath the Aegean inferred from SKS splitting observations, *J. geophys. Res.,* **116,** B04314, doi:10.1029/2010JB007884.

Gallart, J. *et al.*, 2012. Crustal structure beneath the Rif Cordillera, North Morocco, from active seismic profiling, *Geophys. Res. Abstr.,* **14**, EGU2012-5847.

Gallastegui, J., Pulgar, J.A. & Gallart, J., 2002. Initiation of an active margina at North Iberian continent-ocean transition, *Tectonics,* **21**, doi:10.1029/2001TC901046.

Garcia-Castellanos, D. & Villaseñor, A., 2011. Messinian salinity crisis regulated by competing tectonics and erosion at the Gibraltar Arc., *Nature,* **480,** 359–363.

Giacomuzzi, G., Civalleri, M., De Gori, P. & Chiarabba, C., 2012. A 3D Vs model of the upper mantle beneath Italy: insight on the geodynamics of central Mediterranean, *Earth planet. Sci. Lett.,* **335–336,** 105–120.

Grad, M. & Tiira, T. and ESC Working Group, 2009. The Moho depth map of the European Plate, *Geophys. J. Int.,* **176,** 279–292.

Hearn, T.M., 1996. Anisotropic Pn tomography in the western United States, *J. geophys. Res.,* **101**(B2), 8403–8414.

Hearn, T.M., 1999. Uppermost mantle velocities and anisotropy beneath Europe, *J. Geophys.,* **104**(B7), 15 123–15 139.

Hearn, T.M. & Ni, J.F., 1994. Pn velocities beneath continental collision zones: the Turkish-Iranian Plateau, *Geophys. J. Int.,* **117,** 273–283.

International Seismological Centre, 2010. On-line BulletinInternatl. Seis. Cent., Thatcham, United Kingdom. Available at: http://www.isc.ac.uk (23 November 2011, date last accessed).

Karato, S.I. & Jung, H., 1998. Water, partial melting and the origin of the seismic low velocity and high velocity zone in the upper mantle, *Earth planet. Sci. Lett.,* **157,** 193–207.

Koulakov, I., Kaban, M.K., Tesauro, M. & Cloetingh, S., 2009. P- and S-velocity anomalies in the upper mantle beneath Europe from tomographic inversion of ISC data, *Geophys. J. Int.,* **179,** 345–366.

Legendre, C.P., Meier, T., Lebedev, S., Friederich, W & Viereck-Göttel, L., 2012. A shear wave velocity model of the European upper mantle from automated inversion of seismic shear and surface waveforms, *Geophys. J. Int.,* **191,** 282–304.

Lippitsch, R., Kissling, E. & Ansorge, J., 2003. Upper mantle structure beneath the Alpine orogen from high resolution teleseismic tomography, *J. geophys. Res.,* **108**(B8), 2376, doi:10.1029/2002JB002016.

Marone, F., van der Lee, S. & Giardini, D., 2004. Three-dimensional upper mantle S-velocity model for the Eurasia-Africa plate boundary region, *Geophys. J. Int.,* **158**(1), 109–130.

Mauffret, A., Frizon de Lamotte, D., Lallemant, S., Gorini, C. & Maillard, A., 2004. E-W opening of the Algerian Basin (Western Mediterranean), *Terra Nova,* **16,** 257–264.

Mele, G., Rovelli, D., Seber, D, Hearn, T & Barazangi, M, 1998. Compressional velocity structure and anisotropy in the uppermost mantle beneath Italy and surrounding regions, *J. Geophys. Res.,* **103,** 12529–12543.

Muñoz, J.A., 1992. Evolution of a continental collision belt: ECORS-Pyrenees crustal balanced cross section, in *Thrust Tectonics*, pp. 235–246, ed. McClay, K., Chapman and Hall, New York.

Mutlu, A.K. & Karabulut, H., 2011. Anisotropic Pn tomography of Turkey and adjacent regions, *Geophys. J. Int.*, **187**(3), 1743–1758.

Nicolas, A. & Christensen, N.I., 1987. Formation of anisotropy in upper-mantle peridotites—a review, in Froidevaux, C. & Fuchs, K. (eds), The composition, Structure and Dynamics of the Lithosphere-Asthenosphere System, American Geophysical Union Geodynamics Series, pp. 111–123.

Paige, C .C. & Saunders, M.A., 1982. LSQR: An algorithm for sparse linear equations and sparse linear systems, *ACM Trans. Math. Software,* **8,** 43–71.

Pei, S., Sun, Y. & Toksöz, M.N., 2011a. Tomographic Pn and Sn velocity beneath the continental collision zone from Alps to Himalaya, *J. geophys. Res.,* **116**(B10311), doi:10.1029/2010JB007845.

Pei, S., Sun, Y., Toksöz, M.N., Chen, Y.J., Gao, X., Wang, Z., Zhao, J. & Liu, H., 2011b. Imaging Poisson's ratio of the uppermost mantle beneath China, *Bull. seism. Soc. Am.,* **101**(3), 1452–1461.

Platt, J.P., Becker, Th. W., Evans, R.L., Humphreys, E.D., Lee, C.-T. & Levander, A., 2008. PICASSO: testing models for upper mantle processes beneath the Alboran Basin and the Gibraltar Arc (Western Mediterranean), *Geol. Soc. Am. Abstr. Prog.,* **40**(6), 273.

Piromallo, C. & Morelli, A., 2003. P wave tomography of the mantle under the Alpine-Mediterranean area, *J. geophys. Res.,* **108**(B2), 2065, doi:10.1029/2002JB001757.

Rosenbaum, G., Lister, G.S. & Duboz, C., 2002. Reconstruction of the tectonic evolution of the western Mediterranean since the Oligocene, in *Reconstruction of the Evolution of the Alpine-Himalayan Orogen*, eds Rosenbaum, G. & Lister, G.S. [*Journal of the Virtual Explorer*, Vol. **8,** 107–130].

Salimbeni, S., Pondrelli, S., Margheriti, L., Park, J. & Levin, V., 2008. SKS splitting measurements beneath Northern Apennines region: a case of oblique trench-retreat, *Tectonophysics,* **462,** 68–82.

Sato, H., Sacks, I.S. & Murase, T., 1989. The use of laboratory velocity data for estimating temperature and partial melt fraction in the low-velocity zone: comparison with heat flow and electrical conductivity studies, *J. geosphys. Res.,* **94**(B5), 5689–5704.

Schmid, Ch., Van Der Lee, S. & Giardini, D., 2004. Delay times and shear wave splitting in the Mediterranean region, *Geophys. J. Int.,* **159**(1), 275–290.

Schmid, C., van der Lee, S., VanDecar, J.C., Engdahl, E.R. & Giardini, D., 2008. Three-dimensional S velocity of the mantle in the Africa-Eurasia plate boundary region from phase arrival times and regional waveforms, *J. geophys. Res.,* **113,** B03306, doi:10.1029/2005JB004193.

Serrano, I., Hearn, T.M., Morales, J. & Torcal, F., 2005. Seismic anisotropy and velocity structure beneath the southern half of the Iberian Peninsula, *Phys. Earth planet. Inter.,* **150,** 317–330.

Song, L.-P., Koch, M., Koch, K. & Schlittenhardt, J., 2004. 2-D anisotropic Pn-velocity tomography underneath Germany using regional traveltimes, *Geophys. J. Int.,* **157,** 645–663.

Soto, J.I., Fernández-Ibáñez, F., Fernàndez, M. & García-Casco, A., 2008. Thermal structure of the crust in the Gibraltar Arc: Influence on active tectonics in the western Mediterranean, *Geochem. Geophys. Geosyst.,* **9,** Q10011, doi:10.1029/2008GC002061.

Teixell, A., 1998. Crustal structure and orogenic material budget in west central Pyrenees, *Tectonics,* **17,** 395–406.

Tesauro, M., Kaban, M.K. & Cloetingh, S.A.P.L., 2008. EuCRUST-07: a new reference model for the European crust, *Geophys. Res. Lett.,* **35,** L05313, doi:10.1029/2007GL032244.

Vergés, J. *et al.*, 1995. Eastern Pyrenees and related foreland basins: Pre-, syn- and post-collisional crustalscale cross-sections, *Mar. Pet. Geol.,* **12,** 893–915.

Wessel, P. & Smith, W.H.F., 1998. New, improved version of the generic mapping tool released, *Eos, Trans. Am. geophys. Un.,* **47,** 576.

Wüstefeld, A., Bokelmann, G.H.R., Barruol, G. & Montagner, J.-P., 2009. Identifying global seismic anisotropy patterns by correlating shear-wave splitting and surface waves data, *Phys. Earth planet. Int*. **176**(3–4), 198–212.

Zhu, H., Bozdag, E., Peter, D. & Tromp, J., 2012. Structure of the European upper mantle revealed by adjoint tomography, *Nat. Geosci.,* **5,** 493–498.